PAPER

Mechanisms of temperature-dependent oxygen absorption/release and appearance of intermediate phase in κ-Ce₂Zr₂O₈: study based on oxygen vacancy formation energy computations†

Hirotoshi Hirai 🆔 * and Ryosuke Jinnouchi

This study clarified the mechanisms of the temperature-dependent oxygen absorption/release properties and appearance of the intermediate phase for κ-Ce₂Zr₂O₈, which is known to have a high oxygen storage/release capacity (OSC). First-principle computations revealed that the vacancy formation energies depend on the number of vacancies and can be categorized into two groups: low-energy and high-energy. The intermediate phase observed experimentally was assigned to the state after all the oxygen vacancies in the low-energy group were formed. We also found that the mechanism of the improved OSC performance by Ti substitution could be explained in terms of the vacancy formation energies.

1 Introduction

Oxygen storage/release materials have been actively investigated in a wide variety of fields, including environmental protection[1] and energy conversion.[2] In these fields, ceria (CeO₂)-based materials are known to have high oxygen storage/release capacities (OSCs) and are used in industrial applications such as automobile three-way catalysts,[3–5] water–gas shift reactions,[6] and solid oxide fuel cells.[7] In automobile three-way catalysts, ceria-based materials are used as oxygen storage/release materials to adequately control the oxygen concentration on the catalyst surfaces by storing oxygen in an oxidized atmosphere and releasing it under a reduced atmosphere.[3,5,8] Among the ceria-based materials, cation-ordered Ce₂Zr₂O₈ (κ-Ce₂Zr₂O₈) has been reported to have an outstanding OSC, where almost all the Ce atoms contribute to the redox conversion.[9–11] The mechanism of the high OSC performance of κ-Ce₂Zr₂O₈ has been studied both experimentally[12,13] and theoretically.[14,15] These studies have clarified that oxygen vacancies are formed at oxygen sites coordinated only with Zr atoms, even though the binding strength of Zr⁴⁺–O²⁻ is usually stronger than that of Ce⁴⁺–O²⁻. The oxygen vacancy formation energy is known to be dominated by the structural relaxations that occur after the formation of oxygen vacancies. In κ-Ce₂Zr₂O₈, when the Zr⁴⁺–O²⁻ bond is broken and an oxygen vacancy is formed, the remaining oxygen atoms move toward the vacancy sites as

a result of the driving force caused by the differences in the electrostatic forces and ionic radii of Zr and Ce. The oxygen vacancies at the Zr sites are stabilized by this relaxation. Simultaneously, the valency of Zr is retained at 4+ by electron transfer *via* the redox reaction of Ce from 4+ to 3+. This electron transfer prevents the significant movement of Zr atoms, and therefore, the energetically unfavorable lattice distortion is minimized. This latter feature enables the topotactic transformation of κ-Ce₂Zr₂O₈ into Ce₂Zr₂O₇ pyrochlore by maximizing the locality of the structural relaxation.[14] In theoretical studies, the oxygen vacancy formation energies were examined using density functional theory (DFT) calculations and used to understand the atomic-scale structural changes and oxygen vacancy formation properties.[14,15] Experimental analyses also clarified the presence of the intermediate phase, β-Ce₂Zr₂O₇.₅, in the space group $F\bar{4}3m$ between the κ-Ce₂Zr₂O₈ ($Fm\bar{3}m$) and Ce₂Zr₂O₇ pyrochlore ($Fd\bar{3}m$) states.[13,16] The existence of the intermediate state results in the two-step oxygen absorption/release behavior observed during heating under an oxidized/reduced atmosphere.[16] Recently, Ti substitution in Ce₀.₅Ti_xZr₀.₅₋ₓO₂ was found to greatly enhance the OSC performance.[17] Ce₀.₅Ti₀.₁Zr₀.₄O₂ was found to have approximately twice the OSC value of κ-Ce₂Zr₂O₈ at a lower temperature (473 K). A bond valence sum (BVS) analysis[18,19] showed that this OSC enhancement could be explained by the formation of weakly bound oxygen atoms.[17] However, despite the efforts made in this field, the mechanisms of the appearance of the intermediate phase and the two-step oxygen absorption/release behavior have not yet been fully explained. The mechanism of the OSC enhancement by Ti substitution is also unclear.

Toyota Central R&D Labs, Inc., Yokomichi 41-1, Nagakute, Aichi 480-1192, Japan. E-mail: hirotosih@mosk.tytlabs.co.jp

In this study, we systematically investigated the formation of oxygen vacancies from a fully oxidized state (κ-$Ce_2Zr_2O_8$) to a fully reduced state ($Ce_2Zr_2O_7$ pyrochlore) using DFT, including the Hubbard-U term (DFT+U).[20,21] The same method was applied to Ti-substituted systems.

The systematic computations of the oxygen vacancy formation energies revealed that they depended on the number of vacancies and could be categorized into two groups: low- and high-energy. The intermediate phase obtained experimentally was assigned to the state after all the oxygen vacancies in the low-energy group were formed. The theoretical conclusion was verified by comparing the simulated X-ray diffraction (XRD) spectra with the experimental results. This new finding reasonably explained the two-step oxygen absorption/release behavior observed in the experiments. The OSC enhancement at low temperatures by Ti substitution was also reasonably explained by the oxygen vacancy formation energy computations.

2   Method

2.1   First-principle computations

The periodic DFT method was used for the electronic structure computations. The computations were performed using the vienna *ab initio* simulation package (VASP).[22,23] The generalized gradient approximation (GGA) of the Perdew–Burke–Ernzerhof (PBE) functional[24] was used to describe the exchange–correlation interaction of electrons. The projector-augmented wave (PAW) method[25] was used to describe the core–valence interaction. GGA cannot accurately describe the electronic structure of reduced ceria-based materials because of the presence of the self-interaction error.[20,26–28] Therefore, an on-site Coulomb correction was included using the DFT+U method[29] to properly incorporate the behavior of Ce 4f electrons. The previous study showed that significant delocalisation because of the self-interaction error that remained for $U < 5$ eV, while the results were converged for $U \geq 5$ eV where the localisation was found to be independent of the choice of U.[20,26] The similar oxygen vacancy formation energies of CeO_2 have been reported for U greater than 5 eV (3.15, 3.19, 3.20 eV for $U = 5$, 6.1, 6.3 eV, respectively).[15,20,26] Therefore, the value of U was set to 5 eV in this study. Spin-polarized calculations were performed to correctly treat the sub-stoichiometric oxygen. The cut-off energy of the plane wave was set to 400 eV, which has been validated for the $CeZrO_2$ system.[15] The k-point sampling was performed using a $2 \times 2 \times 2$ Monkhorst-Pack mesh, except for the calculation of gas-phase oxygen molecules, which was performed using the Γ point and a cubic unit cell with 10 Å per side. Both the lattice and atomic positions were fully relaxed to obtain a stable structure. No symmetries were applied to the structural optimization. To investigate the OSC mechanism in detail, Bader charge analysis was performed using the code of Henkelman *et al.*[30]

2.2   Model systems

The 96 atom super cell ($Ce_{16}Zr_{16}O_{64}$) shown in Fig. 1 was used for the κ-$Ce_2Zr_2O_8$ computations. The 64 oxygen atoms in the 96 atom super cell can be classified into three types: 8 O_a
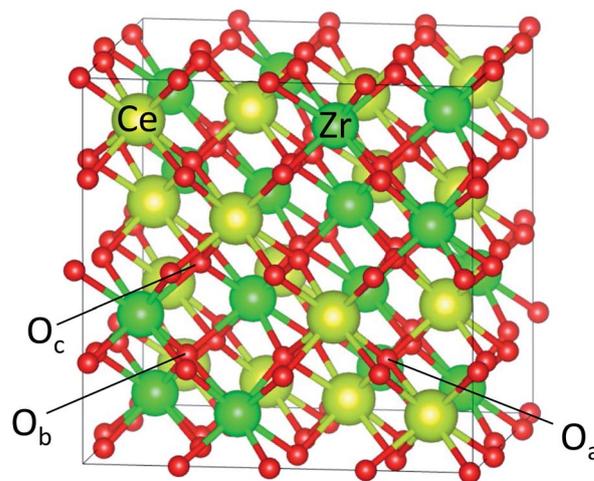

Fig. 1 Super cell of $Ce_{16}Zr_{16}O_{64}$ (96 atoms) for κ-$Ce_2Zr_2O_8$. The cations (Ce^{4+} and Zr^{4+}) were ordered. Examples of three types of oxygen atoms, O_a, O_b, and O_c, are indicated.

(coordinated only with Ce), 8 O_b (coordinated only with Zr), and 48 O_c (coordinated with both Ce and Zr atoms),[10–12] as shown in Fig. 1. Oxygen vacancies are known to preferentially form at O_b sites.[12,14] When all 8 O_b atoms are removed (complete reduction), the remaining 88 atom unit cell represents $Ce_2Zr_2O_7$ pyrochlore.

To model the Ti-substituted system, we selected a $Ce_{16}Ti_2Zr_{14}O_{64}$ system. The Ti cation ratio of this system (6.25 mol%) was close to the composition that exhibited a significant OSC improvement in an experiment (9.7 mol%).[17] A Ti-substituted system was experimentally confirmed to have a cation-ordered structure.[17] The preferential vacancy formation sites were considered to be the same as those in the κ-$Ce_2Zr_2O_8$ system. The formation of oxygen vacancies was expected to be activated by Ti substitution because the Ti–O bond is weaker than the Zr–O bond as a result of the greater electronegativity of Ti^{4+} (the electronegativities estimated by the empirical model[31] were 1.73 and 1.61 for Ti^{4+} and Zr^{4+}, respectively). Therefore, 8 O_b sites were chosen as vacancy formation sites. The remaining task was to determine the Ti substitution sites.

Several combinations of Zr sites can be replaced by Ti atoms. We examined the calculated total energies of all the symmetrically independent combinations of Ti substitution sites to determine the most stable combination (see ESI† for the calculation result). This examination indicated that in the most stable state, with two Ti substitutions, the two substituted Ti atoms were adjacent to each other (see Fig. 2). Because the ionic radius of Ti^{4+} is smaller than that of Zr^{4+} (Zr^{4+}: 0.84 Å, Ti^{4+}: 0.74 Å),[32] the substitution caused a structure distortion around the substituted sites. This distortion could be localized using the configuration shown in Fig. 2 because the induced strain could be cancelled by adjacent substituted Ti atoms. This was considered to be the reason that two substituted Ti atoms energetically preferred the adjacent substitution sites. The oxygen vacancy formation energies of $Ce_{16}Ti_2Zr_{14}O_{64}$ were computed using this atomic configuration.
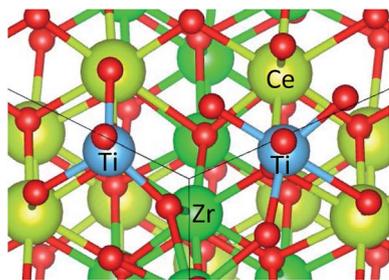

Fig. 2 Optimized Ti-substituted structure for $Ce_{16}Ti_2Zr_{14}O_{64}$ system.

2.3 Oxygen vacancy formation energy

The oxygen vacancy formation energy, E_v^f, relative to the gas-phase O_2 molecule was computed using the following equation:

$$E_v^f(N) = \frac{1}{N}\left(E[N] - E[N=0] + \frac{N}{2}E[O_2^{gas}]\right). \quad (1)$$

Here, N is the number of oxygen vacancies, $E[N]$ is the energy of the bulk with N oxygen vacancies, and $E[O_2^{gas}]$ is the energy of the oxygen molecule in vacuum. As previously described, in the bulk energy calculations, the cell volume, shape, and atomic positions were fully relaxed. Unlike previous studies, where $E_v^f(N)$ was computed only for a discrete number of vacancies ($N = 1$, 4, and 8 in ref. 14), we systematically computed $E_v^f(N)$ for all cases ($N = 1$–8), from the fully oxidized state (κ-$Ce_{16}Zr_{16}O_{64}$) to the fully reduced state ($Ce_{16}Zr_{16}O_{56}$ pyrochlore).

The oxygen vacancy sites in $Ce_{16}Zr_{16}O_{64}$ were assumed to be oxygen atoms coordinated only to Zr atoms (O_b, see Fig. 1). Although all the O_b atoms were symmetrically equivalent for $N = 1$, some of the remaining O_b atoms became inequivalent after the vacancy formation. In this study, the oxygen vacancy formation energies were examined for all symmetrically inequivalent combinations of O_b sites, and the most stable combinations were selected for $E_v^f(N)$. In the case of $Ce_{16}Ti_2Zr_{14}O_{64}$, the O_b atoms, some of which were coordinated to both Zr and Ti atoms, were not symmetrically equivalent even for $N = 1$. The oxygen vacancy formation energies were computed for all the combination patterns of the O_b sites, and the most stable combinations were selected for $E_v^f(N)$.

2.4 Symmetry analysis and XRD pattern simulation

The XRD patterns were simulated using the VESTA program[33] to assign the theoretically obtained structure to the experimentally observed intermediate phase. The FINDSYM program[34] was used to examine the symmetry of the theoretically obtained crystals and compare them with the space group of the intermediate phase. The tolerance parameters of the program were set as follows: lattice: 0.01, position: 0.1, and rotational moment: 0.1.

3 Results and discussion

Fig. 3 shows the computed oxygen vacancy formation energies, $E_v^f(N)$, for κ-$Ce_{16}Zr_{16}O_{64}$ and Ti-substituted $Ce_{16}Ti_2Zr_{14}O_{64}$. For both κ-$Ce_{16}Zr_{16}O_{64}$ and Ti-substituted $Ce_{16}Ti_2Zr_{14}O_{64}$, the

dependence of the formation energy on N appeared to be a sigmoid function, indicating that the $E_v^f(N)$ values could be categorized into two groups: low-energy (first four) and high-energy (last three) groups. The vacancy formation energies of the high-energy group were less than 0.5 eV. These were significantly smaller than those of other materials (e.g., 2.09 eV for tetragonal $Ce_2Zr_2O_8$ (ref. 14)). This indicated that κ-$Ce_2Zr_2O_8$ can release oxygen at relatively low temperatures, making it an excellent OSC material. The oxygen vacancy formation energies at $N = 5$ were between those of the two groups. The locations of the low-energy and fifth vacancy sites are shown in Fig. 4. A close examination of the structure indicated that the four vacancy sites in the low-energy group were at locations that maximized their distances. As reported in the literature,[14] the sacrificial reduction of the surrounding Ce atoms can produce oxygen vacancies with little charge fluctuation of the Zr atoms in the κ-$Ce_2Zr_2O_8$ system. The maximized distances allow Ce atoms to efficiently influence the vacancy sites via the sacrificial reduction mechanism. It should also be noted that the lattice distortions caused by vacancy formation can be minimized by maximizing the distance. Fig. 4 shows that the fifth oxygen vacancy site was located at the center of the four low-energy group sites. This special location was considered to suppress the lattice distortion and make the vacancy formation energy relatively small. However, when additional oxygen vacancies were generated at the high-energy group sites, the symmetry was broken, and the additional vacancy sites had to be adjacent to the existing vacancy sites. In these cases, the distance between vacancy sites became significantly shorter. Therefore, the additional vacancy formations could not benefit from the sacrificial reduction of Ce atoms, and the lattice distortions became significantly large. Accordingly, the two distinct energy groups were attributed to the symmetry of the vacancy formation sites.

In the experiment,[13] a stable intermediate phase with space group $F\bar{4}3m$ at a composition of $Ce_2Zr_2O_{7.5}$ was observed. In this study, the composition of the intermediate phase ($Ce_{16}Zr_{16}O_{60}$)

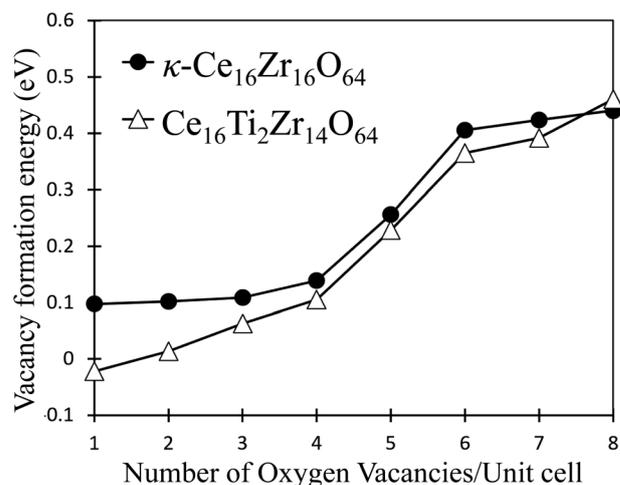**Fig. 3** Vacancy formation energies for κ-$Ce_{16}Zr_{16}O_{64}$ and $Ce_{16}Ti_2Zr_{14}O_{64}$ systems.
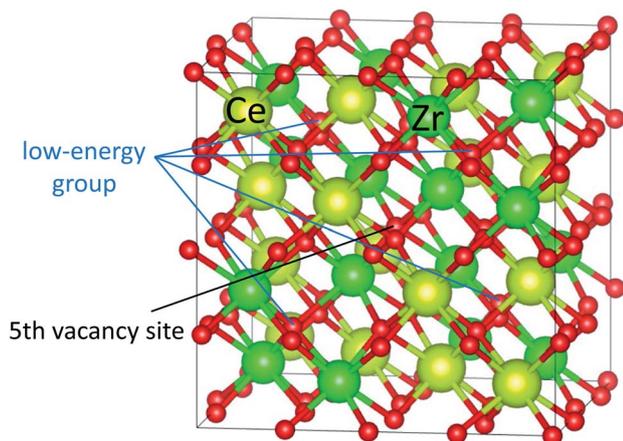
Fig. 4 Locations of vacancy sites for low-energy group and 5th vacancy site.

was assigned to $N = 4$. Therefore, the experimentally observed intermediate phase was considered to be the state after all the oxygen vacancies in the low-energy group were formed. This assignment was supported by the simulated XRD patterns of the structures of $N = 4$ ($Ce_{16}Zr_{16}O_{60}$), $N = 0$ (κ-$Ce_{16}Zr_{16}O_{64}$), $N = 5$ ($Ce_{16}Zr_{16}O_{59}$), and $N = 8$ ($Ce_{16}Zr_{16}O_{56}$ pyrochlore). The simulated XRD patterns are shown in Fig. 5. The peaks with a Miller index of (200), which are characteristic of the experimentally observed intermediate phase,[13] are visible in the XRD patterns of $Ce_{16}Zr_{16}O_{60}$ and $Ce_{16}Zr_{16}O_{59}$, but do not appear in the XRD patterns of $Ce_{16}Zr_{16}O_{56}$ and $Ce_{16}Zr_{16}O_{64}$. For more precise assignments, the space groups were examined for the computed structures of $Ce_{16}Zr_{16}O_{60}$ and $Ce_{16}Zr_{16}O_{59}$. The space group of $Ce_{16}Zr_{16}O_{60}$ was identified as $F\bar{4}3m$, which corresponded to the experimentally detected space group of the intermediate phase, whereas that of $Ce_{16}Zr_{16}O_{59}$ was identified as $P\bar{4}3m$. Hence, the experimentally observed intermediate phase was assigned to the state after all the oxygen vacancies were formed at the low-
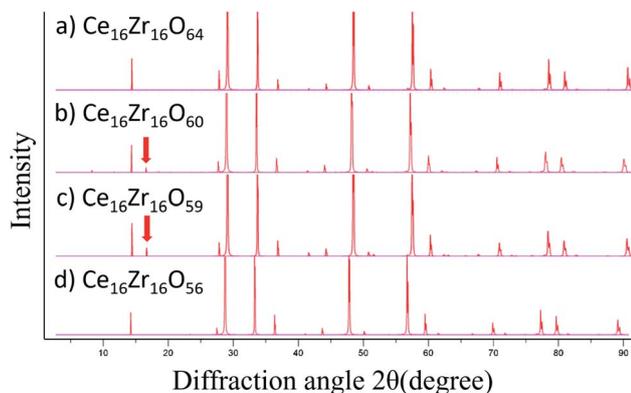
energy group sites. The theoretically obtained formation energy gap between the low- and high-energy groups, as shown in Fig. 3, explains the stability of this intermediate phase.

As shown in Fig. 3, the oxygen vacancy formation energies in the low-energy group were reduced by Ti substitution, whereas no significant change was observed in the high-energy group. This indicated that the release temperatures of the oxygen atoms at the low-energy group sites decreased. In other words, the amount of oxygen released at low temperatures increased. This feature was consistent with experimental results.[17] Unlike κ-$Ce_{16}Zr_{16}O_{64}$, the eight oxygen sites, O_b, in the $Ce_{16}Ti_2Zr_{14}O_{64}$ system are not equivalent because of the Ti substitution. Based on the electronegativities of Ti (1.54) and Zr (1.33), we expected that oxygen atoms directly coordinated to Ti would be more easily released than oxygen atoms coordinated only to Zr because oxygen cannot take as many electrons from Ti as Zr. This expectation could be true if vacancies were formed without any structural relaxation, as verified by our preliminary DFT+U calculations on frozen structures. However, when the lattice relaxation was switched on, the vacancy formation energy for the oxygen atoms coordinated only to Zr was smaller than that of Ti. This stemmed from the large strain caused by the removal of oxygen coordinated directly by Ti, which has a smaller ionic radius than Zr.

Although oxygen vacancies were formed at the Zr sites regardless of the Ti substitution, the oxygen vacancy formation energies were significantly reduced by the Ti substitution. To investigate the mechanism of this reduction, Bader charge analyses were conducted for $Ce_{16}Ti_2Zr_{14}O_{64}$ and κ-$Ce_{16}Zr_{16}O_{64}$. The electron numbers obtained by these Bader charge analyses for all the atoms before and after the first oxygen vacancy formation are compared in Fig. 6. The sacrificial reduction of Ce atoms was observed in the κ-$Ce_{16}Zr_{16}O_{64}$ system, where the electron numbers of three specific Ce atoms increased when an oxygen vacancy was formed. The reduced Ce sites formed a triangle around the vacancy sites (inset in Fig. 6). However, the electron numbers of Zr atoms, which involved Zr atoms directly coordinating the oxygen vacancy sites, did not change significantly. This result was consistent with that of a previous study,[14] although two Ce atoms instead of three were reduced during the oxygen vacancy formation in past calculations, where the supercell was fixed during the calculations. This number difference was attributed to the relaxation of the supercell: two Ce atoms were reduced when the supercell was fixed in our preliminary calculations. In contrast, in $Ce_{16}Ti_2Zr_{14}O_{64}$ systems, the electron amounts for the Ce atoms were already increased with the Ti substitution before the vacancy formation, as shown in Fig. 6. These electrons were confirmed to originate from the oxygen atoms (the Bader charge for the oxygen atoms was decreased by the Ti substitution). However, the number of electrons in the Zr atoms was not affected. The decrease in the number of oxygen electrons resulted in a decrease in the strength of the ionic bonds. This was considered to be the cause of the decrease in the oxygen vacancy formation energies.

Fig. 5 Simulated XRD patterns for (a) $Ce_{16}Zr_{16}O_{64}$, (b) $Ce_{16}Zr_{16}O_{60}$, (c) $Ce_{16}Zr_{16}O_{59}$, and (d) $Ce_{16}Zr_{16}O_{56}$. The peaks corresponding to a Miller index of (200), which is characteristic of the intermediate phase, are highlighted by arrows.

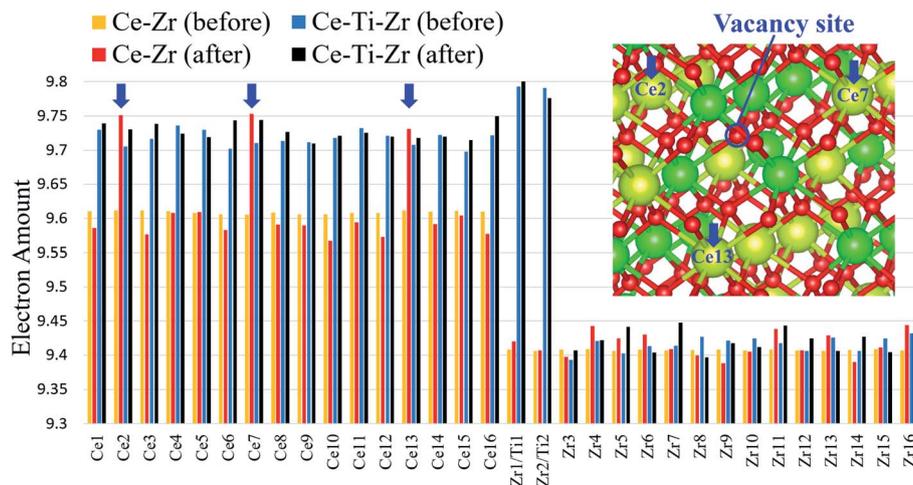**Fig. 6** Bader charge amounts for each cation before and after oxygen vacancy formation for κ-$Ce_{16}Zr_{16}O_{64}$ and $Ce_{16}Ti_2Zr_{14}O_{64}$ systems. Three specific reduced Ce atoms are indicated by blue arrows, and their positions are shown in the inset.

4 Conclusion

In this study, we systematically investigated the formation of oxygen vacancies from the fully oxidized state (κ-$Ce_2Zr_2O_8$) to the fully reduced state ($Ce_2Zr_2O_7$ pyrochlore) using first-principles computations based on the DFT+U method. Systematic computations of the oxygen vacancy formation energies of cation-ordered $Ce_2Zr_2O_8$ revealed that the arrangement of vacancy sites was determined so that the distance between vacancy sites was as large as possible, and the symmetry was as high as possible. This ordered arrangement minimized the lattice distortion and maximized the benefit of Ce reduction during the vacancy formation. This feature resulted in the appearance of two oxygen vacancy formation energy groups: low- and high-energy groups. The intermediate phase obtained experimentally was assigned to the state after all the oxygen vacancies in the low-energy group were formed on the basis of the simulated XRD spectra. The theoretically obtained oxygen vacancy energies explained the two-step oxygen absorption/release behavior observed experimentally during heating under oxidized and reduced atmospheres. In addition, this ordered vacancy formation was considered to be one of the reasons for the possibility of topotactic transformation between κ-$Ce_2Zr_2O_8$ and $Ce_2Zr_2O_7$ pyrochlore. The OSC enhancement by Ti substitution at lower temperatures was also reproduced by the theoretical oxygen vacancy formation energies. The charge transfer from oxygen atoms to Ce atoms caused by the Ti substitution was considered to be the main factor for the improved OSC.

Conflicts of interest

The authors declare that they have no conflicts of interest.

Acknowledgements

References

1 S. Carrettin, P. Concepción, A. Corma, J. M. Lopez Nieto and V. F. Puntes, Nanocrystalline CeO2 increases the activity of Au for CO oxidation by two orders of magnitude, *Angew. Chem., Int. Ed.*, 2004, **43**(19), 2538–2540.

2 G. A. Deluga, J. R. Salge, L. D. Schmidt and X. E. Verykios, Renewable hydrogen from ethanol by autothermal reforming, *Science*, 2004, **303**(5660), 993–997.

3 A. F. Diwell, R. R. Rajaram, H. A. Shaw and T. J. Truex, The role of ceria in three-way catalysts, in *Studies in Surface Science and Catalysis*, Elsevier, 1991, vol. 71, pp. 139–152.

4 J. Kašpar, P. Fornasiero and M. Graziani, Use of CeO2-based oxides in the three-way catalysis, *Catal. Today*, 1999, **50**(2), 285–298.

5 J. Kašpar and P. Fornasiero, Nanostructured materials for advanced automotive de-pollution catalysts, *J. Solid State Chem.*, 2003, **171**(1–2), 19–29.

6 Q. Fu, H. Saltsburg and M. Flytzani-Stephanopoulos, Active nonmetallic Au and Pt species on ceria-based water-gas shift catalysts, *Science*, 2003, **301**(5635), 935–938.

7 Z. Xu, Z. Qi and A. Kaufman, Effect of oxygen storage materials on the performance of proton-exchange membrane fuel cells, *J. Power Sources*, 2003, **115**(1), 40–43.

8 P. Li, X. Chen, Y. Li and J. W. Schwank, A review on oxygen storage capacity of CeO2-based materials: Influence factors, measurement techniques, and applications in reactions related to catalytic automotive emissions control, *Catal. Today*, 2019, **327**, 90–115.

9 Y. Nagai, T. Yamamoto, T. Tanaka, S. Yoshida, T. Nonaka, T. Okamoto, A. Suda and M. Sugiura, X-ray absorption fine structure analysis of local structure of CeO2–ZrO2 mixed oxides with the same composition ratio (Ce/Zr=1), *Catal. Today*, 2002, **74**(3–4), 225–234.

10 H. Kishimoto, T. Omata, S. Otsuka-Yao-Matsuo, K. Ueda, H. Hosono and H. Kawazoe, Crystal structure of metastable κ-CeZrO4 phase possessing an ordered

arrangement of Ce and Zr ions, *J. Alloys Compd.*, 2000, **312**(1–2), 94–103.

11 A. Suda, Y. Ukyo, H. Sobukawa and M. Sugiura, Improvement of oxygen storage capacity of CeO$_2$–ZrO$_2$ solid solution by heat treatment in reducing atmosphere, *J. Ceram. Soc. Jpn.*, 2002, **110**(1278), 126–130.

12 T. Yamamoto, A. Suzuki, Y. Nagai, T. Tanabe, F. Dong, Y. Inada, M. Nomura, M. Tada and Y. Iwasawa, Origin and dynamics of oxygen storage/release in a Pt/ordered CeO$_2$–ZrO$_2$ catalyst studied by time-resolved XAFS analysis, *Angew. Chem., Int. Ed.*, 2007, **46**(48), 9253–9256.

13 T. Sasaki, Y. Ukyo, K. Kuroda, S. Arai, S. Muto and H. Saka, Crystal Structure of Ce$_2$Zr$_2$O$_7$ and β-Ce$_2$Zr$_2$O$_{7.5}$, *J. Ceram. Soc. Jpn.*, 2004, **112**(8), 440–444.

14 H.-F. Wang, Y.-L. Guo, G.-Z. Lu and P. Hu, Maximizing the Localized Relaxation: The Origin of the Outstanding Oxygen Storage Capacity of κ-Ce$_2$Zr$_2$O$_8$, *Angew. Chem., Int. Ed.*, 2009, **48**(44), 8289–8292.

15 H.-T. Chen and J.-G. Chang, Oxygen vacancy formation and migration in Ce$_{1-x}$Zr$_x$O$_2$ catalyst: A DFT+U calculation, *J. Chem. Phys.*, 2010, **132**(21), 214702.

16 T. Sasaki, Y. Ukyo, A. Suda, M. Sugiura, K. Kuroda, S. Arai and H. Saka, Oxygen Absorption Behavior of Ce$_2$Zr$_2$O$_{7+x}$ and Formation of Ce$_2$Zr$_2$O$_{7.5}$, *J. Ceram. Soc. Jpn.*, 2003, **111**(1294), 382–385.

17 Y. Goto, A. Morikawa, M. Iwasaki, M. Miura and T. Tanabe, Enhanced oxygen storage capacity of cation-ordered cerium–zirconium oxide induced by titanium substitution, *Chem. Commun.*, 2018, **54**(28), 3528–3531.

18 I. D. Brown and D. Altermatt, Bond-valence parameters obtained from a systematic analysis of the inorganic crystal structure database, *Acta Crystallogr., Sect. B: Struct. Sci.*, 1985, **41**(4), 244–247.

19 N. E. Brese and M. O'keeffe, Bond-valence parameters for solids, *Acta Crystallogr., Sect. B: Struct. Sci.*, 1991, **47**(2), 192–197.

20 M. Nolan, S. C. Parker and G. W. Watson, The electronic structure of oxygen vacancy defects at the low index surfaces of ceria, *Surf. Sci.*, 2005, **595**(1–3), 223–232.

21 S. Fabris, G. Vicario, G. Balducci, S. de Gironcoli and S. Baroni, Electronic and atomistic structures of clean and reduced ceria surfaces, *J. Phys. Chem. B*, 2005, **109**(48), 22860–22867.

22 G. Kresse and J. Furthmüller, Efficient iterative schemes for ab initio total-energy calculations using a plane-wave basis set, *Phys. Rev. B: Condens. Matter Mater. Phys.*, 1996, **54**(16), 11169.

23 J. Hafner, Materials simulations using VASP—a quantum perspective to materials science, *Comput. Phys. Commun.*, 2007, **177**(1–2), 6–13.

24 J. P. Perdew, K. Burke and M. Ernzerhof, Generalized gradient approximation made simple, *Phys. Rev. Lett.*, 1996, **77**(18), 3865.

25 P. E. Bliichl, Projector augmented-wave method, *Phys. Rev. B: Condens. Matter Mater. Phys.*, 1994, **50**(24), 17953–17979.

26 M. Nolan, S. Grigoleit, D. C. Sayle, S. C. Parker and G. W. Watson, Density functional theory studies of the structure and electronic structure of pure and defective low index surfaces of ceria, *Surf. Sci.*, 2005, **576**(1–3), 217–229.

27 H.-T. Chen, J.-G. Chang, H.-L. Chen and S.-P. Ju, Identifying the O2 diffusion and reduction mechanisms on CeO$_2$ electrolyte in solid oxide fuel cells: a DFT+ U study, *J. Comput. Chem.*, 2009, **30**(15), 2433–2442.

28 G. Vicario, G. Balducci, S. Fabris, S. de Gironcoli and S. Baroni, Interaction of hydrogen with cerium oxide surfaces: a quantum mechanical computational study, *J. Phys. Chem. B*, 2006, **110**(39), 19380–19385.

29 M. Cococcioni and S. De Gironcoli, Linear response approach to the calculation of the effective interaction parameters in the LDA+ U method, *Phys. Rev. B: Condens. Matter Mater. Phys.*, 2005, **71**(3), 035105.

30 W. Tang, E. Sanville and G. Henkelman, A grid-based Bader analysis algorithm without lattice bias, *J. Phys.: Condens. Matter*, 2009, **21**(8), 084204.

31 J. Portier, G. Campet, J. Etourneau and B. Tanguy, A simple model for the estimation of electronegativities of cations in different electronic states and coordinations, *J. Alloys Compd.*, 1994, **209**(1–2), 285–289.

32 R. D. Shannon, Revised effective ionic radii and systematic studies of interatomic distances in halides and chalcogenides, *Acta Crystallogr., Sect. A: Cryst. Phys., Diffr., Theor. Gen. Crystallogr.*, 1976, **32**(5), 751–767.

33 K. Momma and F. Izumi, VESTA 3 for three-dimensional visualization of crystal, volumetric and morphology data, *J. Appl. Crystallogr.*, 2011, **44**(6), 1272–1276.

34 H. T. Stokes and D. M. Hatch, FINDSYM: program for identifying the space-group symmetry of a crystal, *J. Appl. Crystallogr.*, 2005, **38**(1), 237–238.